LETTER

A supermassive black hole in an ultra–compact dwarf galaxy

Anil C. Seth[1], Remco van den Bosch[2], Steffen Mieske[3], Holger Baumgardt[4], Mark den Brok[1], Jay Strader[5], Nadine Neumayer[2,6], Igor Chilingarian[7,8], Michael Hilker[6], Richard McDermid[9,10], Lee Spitler[9,10], Jean Brodie[11], Matthias J. Frank[12] & Jonelle L. Walsh[13]

Ultra-compact dwarf galaxies are among the densest stellar systems in the Universe. These systems have masses of up to 2×10^8 solar masses, but half-light radii of just 3–50 parsecs[1]. Dynamical mass estimates show that many such dwarfs are more massive than expected from their luminosity[2]. It remains unclear whether these high dynamical mass estimates arise because of the presence of supermassive black holes or result from a non-standard stellar initial mass function that causes the average stellar mass to be higher than expected[3,4]. Here we report adaptive optics kinematic data of the ultra-compact dwarf galaxy M60-UCD1 that show a central velocity dispersion peak exceeding 100 kilometres per second and modest rotation. Dynamical modelling of these data reveals the presence of a supermassive black hole with a mass of 2.1×10^7 solar masses. This is 15 per cent of the object's total mass. The high black hole mass and mass fraction suggest that M60-UCD1 is the stripped nucleus of a galaxy. Our analysis also shows that M60-UCD1's stellar mass is consistent with its luminosity, implying a large population of previously unrecognized supermassive black holes in other ultra-compact dwarf galaxies[2].

The object M60-UCD1 is the brightest ultracompact dwarf galaxy (UCD) currently known[5], with a V-band luminosity $L_V = 4.1 \times 10^7\, L_\odot$ (where $L_\odot$ is the solar luminosity) and effective radius $r_e = 24$ pc. It lies at a projected distance of 6.6 kpc from the centre of the massive elliptical galaxy M60 (Fig. 1), and 16.5 Mpc from us[6]. We obtained integral field spectroscopic data between $2\,\mu m$ and $2.4\,\mu m$ of M60-UCD1 with the near-infrared integral field spectrograph on the Gemini North telescope. The high-spatial-resolution data obtained using laser guide-star adaptive optics provides a clear detection of the supermassive black hole. Modelling of the deep carbon dioxide (CO) absorption bandheads at $2.3\,\mu m$ enables us to measure the motions of stars at many different points across M60-UCD1. These kinematic measurements are shown in Fig. 2. Two features are particularly notable: (1) the dispersion is strongly peaked, with the central dispersion rising above $100\,\mathrm{km\,s^{-1}}$ and dropping outwards to $\sim 50\,\mathrm{km\,s^{-1}}$, (2) rotation is clearly seen, with a peak amplitude of $40\,\mathrm{km\,s^{-1}}$.

The stellar kinematics can be used to constrain the distribution of mass within M60-UCD1. This includes being able to test whether the mass traces light, or whether a supermassive black hole is required to explain the central velocity dispersion peak. We combined the stellar kinematics and imaging from the Hubble Space Telescope with self-consistent Schwarzschild models[7–9] to constrain the black hole mass and the mass-to-light ratio (M/L, in solar units), shown in Fig. 3. We measure a black-hole mass of $2.1^{+1.4}_{-0.7} \times 10^7\, M_\odot$ and a g-band $M/L = 3.6 \pm 1$ with errors giving 1σ confidence intervals (2σ and 3σ contours are shown in Fig. 3). The total stellar mass is $1.2 \pm 0.4 \times 10^8\, M_\odot$, where $M_\odot$ is the solar mass.

The best-fitting constant-M/L model with no black hole is ruled out with >99.99% confidence.

M60-UCD1 is the lowest-mass system known to host a supermassive black hole ($>10^6\, M_\odot$), including systems with dynamical black hole estimates or with broad-line active galactic nuclei[10,11]. There have been tentative detections of approximately $10^4\, M_\odot$ black holes in lower-mass clusters[12,13]. These detections remain controversial[14,15] and the intermediate-mass black holes, if present, form a much smaller fraction of the total cluster mass than found in M60-UCD1. Of the 75 galaxies with reliable dynamical black hole mass measurements, only one other galaxy has a black hole mass fraction as high as that of M60-UCD1[10,16]. A luminous and variable X-ray source was previously detected in M60-UCD1 with a maximum luminosity of $L_X = 1.3 \times 10^{38}\,\mathrm{ergs\,s^{-1}}$ (ref. 5). This luminosity suggests the black hole is accreting material at a rate typical of black holes in larger, more-massive early-type galaxies as well as other nearby galaxies with absorption-line-dominated optical spectra[17,18].
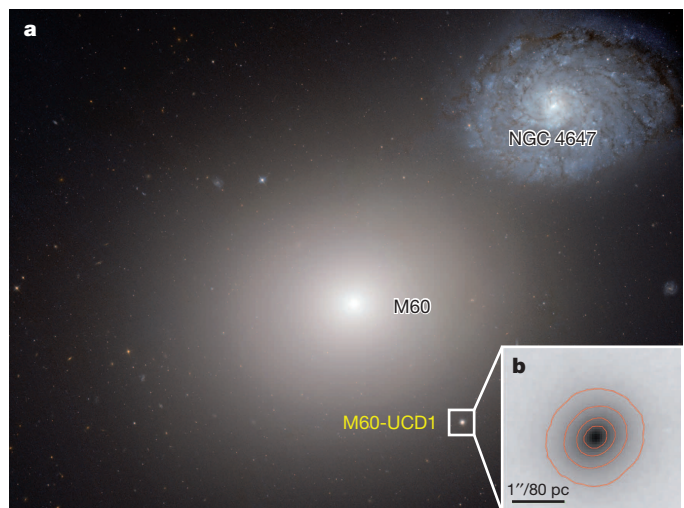

Figure 1 | Hubble Space Telescope image of the M60–NGC 4647 system. M60-UCD1 is the nearly point-like image in the bottom right of **a** (boxed). The discovery of a black hole in M60-UCD1 provides evidence that it is the tidally stripped nucleus of a once larger galaxy. We note that NGC 4647 is at approximately the same distance from Earth as M60 but the two galaxies are not yet strongly interacting. **b**, A zoomed version of the g-band image of M60-UCD1 with contours showing the surface brightness in intervals of one magnitude per square arcsecond. The image is from NASA/ESA.

[1]Department of Physics and Astronomy, University of Utah, 115 South 1400 East, Salt Lake City, Utah 84112, USA. [2]Max-Planck Institut für Astronomie, Königstuhl 17, D-69117 Heidelberg, Germany. [3]European Southern Observatory, Alonso de Cordova 3107, Vitacura, Santiago, 7630355, Chile. [4]School of Mathematics and Physics, University of Queensland, St Lucia, Queensland 4072, Australia. [5]Department of Physics and Astronomy, Michigan State University, East Lansing, Michigan 48824, USA. [6]European Southern Observatory, Karl-Schwarzschild-Strasse 2, 85748 Garching bei München, Germany. [7]Smithsonian Astrophysical Observatory, 60 Garden Street MS09, Cambridge, Massachusetts 02138, USA. [8]Sternberg Astronomical Institute, Moscow State University, 13 Universitetski prospect, Moscow 119992, Russia. [9]Australian Astronomical Observatory, 105 Delhi Road, Sydney, New South Wales 2113, Australia. [10]Department of Physics and Astronomy, Macquarie University, Sydney, New South Wales 2109, Australia. [11]University of California Observatories and Department of Astronomy and Astrophysics, University of California, Santa Cruz, California 95064, USA. [12]Landessternwarte, Zentrum für Astronomie der Universität Heidelberg, Königstuhl 12, D-69117 Heidelberg, Germany. [13]Department of Astronomy, The University of Texas at Austin, 1 University Station C1400, Austin, Texas 78712, USA.
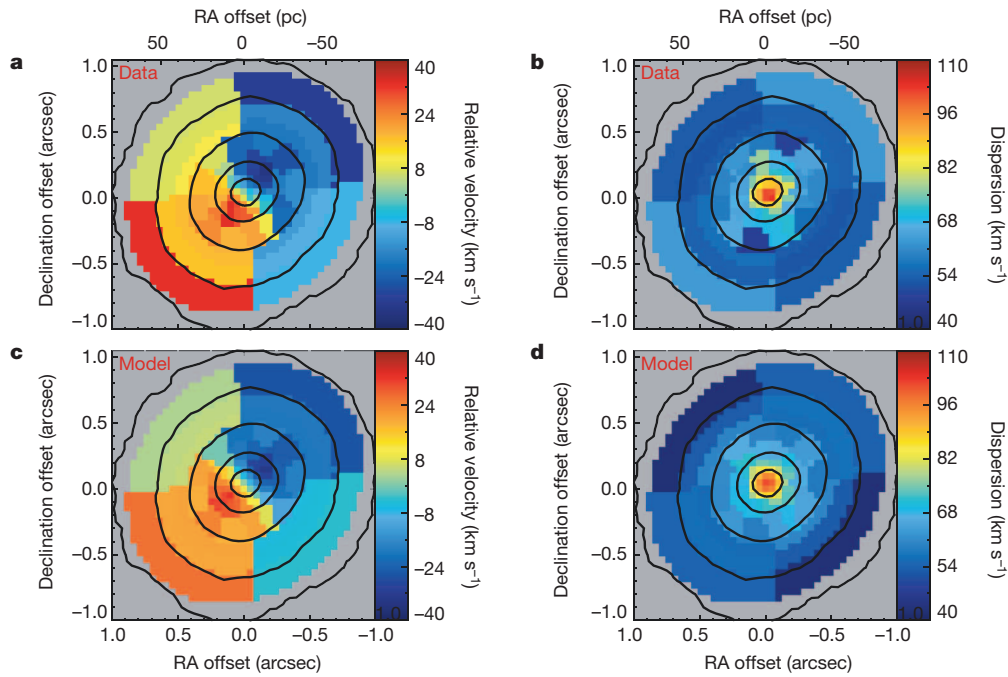
Figure 2 | Stellar kinematic maps of M60-UCD1 showing clear rotation and a dispersion peak. a and **b** show the measured radial velocities (bulk motions towards and away from us) and velocity dispersions (random motions) of the stars in M60-UCD1 with typical errors of 6 km s^{-1}. Black contours show isophotes in the K-band stellar continuum. Kinematics are determined in each individual pixel near the centre, but at larger radii the data were binned to increase the signal-to-noise ratio and enable kinematic measurements. **c** and **d** show the best-fitting dynamical model; a black hole is required to replicate the central dispersion peak.

UCDs are thought to be either the most-massive globular star clusters[19] or nuclei of larger galaxies that have been tidally stripped[20,21]. The super-massive black hole that we have found at the centre of M60-UCD1 provides strong evidence that it is a stripped nucleus of a once larger galaxy. While it is possible that dense star clusters can form black holes, these are expected to contain only a small fraction of the cluster's mass[22]. Star clusters at the centre of galaxy nuclei, on the other hand, are known to host black holes with very high mass fractions[23]. Thus M60-UCD1 is the first individual UCD with explicit evidence for being a tidally stripped nucleus.

We can estimate the properties of M60-UCD1's progenitor galaxy, assuming that they follow scaling relations of present-day unstripped galaxies. Using the known scaling between black hole mass and bulge mass[10], we find a host bulge mass of $7^{+4}_{-3} \times 10^9 \, M_\odot$. Bulge masses are also known to correlate with the masses of their nuclear star clusters[24]. In M60-UCD1, the surface brightness profile has two clear components[5], and we identify the central component as the progenitor nuclear star cluster[21] with mass $6.1 \pm 1.6 \times 10^7 \, M_\odot$. This translates to a predicted bulge mass of $1.8 \pm 0.4 \times 10^{10} \, M_\odot$. Thus, two independent scaling relations suggest that the progenitor bulge mass is about $10^{10} \, M_\odot$. Given M60-UCD1's cluster environment, its progenitor was probably a lower-mass elliptical galaxy that was then stripped by the massive elliptical galaxy M60, which lies at a current projected distance of just 6.6 kpc. We have run simulations that show that it is feasible to produce M60-UCD1 by stripping an elliptical galaxy progenitor of approximately $10^{10} \, M_\odot$ on a fairly radial orbit (see Supplementary Information and Extended Data Fig. 6). We note that current elliptical galaxies of approximately $10^{10} \, M_\odot$ have nuclear star cluster sizes, luminosities and colours consistent with the inner component of M60-UCD1[25,26].

The detection of a supermassive black hole in M60-UCD1 may be just the tip of the iceberg of the UCD black hole population. Measurements of the integrated velocity dispersion in almost all UCDs with masses above $10^7 \, M_\odot$ yield dynamical mass estimates that are too high to be accounted for by a normal stellar population without a massive central black hole[2]. Unlike these previous dynamical mass estimates, our dynamical modelling can separate out the gravitational influence of the black hole from the contribution of the stars. The models show that M60-UCD1's stellar populations appear normal. The mass-to-light ratio of a stellar population characterizes the average mass of its stars. In M60-UCD1 we measured a stellar dynamical mass-to-light ratio in the g band of $M/L_g = 3.6 \pm 1.0$ in solar units (1σ errors). This mass-to-light ratio is consistent with the stellar populations seen in lower-mass globular clusters[27] and models with a normal (Milky Way) initial mass function[28]. It is also lower than the integrated dynamical mass-to-light ratio estimates
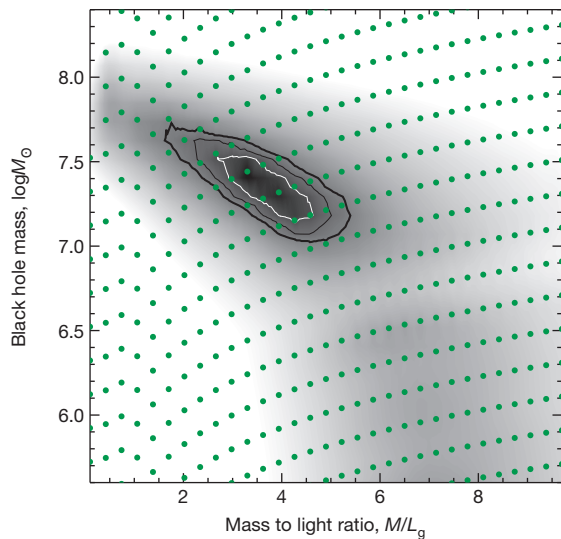

Figure 3 | Dynamical modelling results show the presence of a supermassive black hole. The figure shows goodness-of-fit contours for the dynamical models of M60-UCD1 with two parameters, the g-band mass-to-light ratio and the black hole mass. The contours indicate 1σ (white), 2σ, 3σ (black, thick) confidence levels for two degrees of freedom. Green dots indicate discrete values of the mass-to-light ratio and the black hole mass at which models were fitted to the data.

in 18 of 19 UCDs above $10^7\,M_\odot$ (ref. 2). The low stellar mass-to-light ratio in M60-UCD1 is inconsistent with proposed scenarios in which a density-dependent initial mass function yields higher than normal mass-to-light ratios[4]. Without such a mechanism, the simplest explanation for the high dynamical mass estimates in massive UCDs is that most host supermassive black holes just as M60-UCD1 does.

There is also more limited evidence for enhanced dynamical mass-to-light ratios in lower-mass UCDs. About half of UCDs with masses between $3 \times 10^6\,M_\odot$ and $10^7\,M_\odot$ have higher inferred mass-to-light ratios than we see in M60-UCD1[2]. Taken in combination with tentative black hole detections of about $10^4\,M_\odot$ in Local Group globular clusters[12,13] (which do not have increased M/L values owing to much lower black hole mass fractions), these observations suggest that some lower-mass UCDs may also host relatively massive black holes.

Finally, we estimate what the total population of UCD black holes might be in the local Universe. The most complete sample of known UCDs is in the Fornax cluster. Comparing the UCD population to the population of galaxies in Fornax likely to host massive black holes, we find that UCDs may more than double the number of black holes (see Supplementary Information). Thus UCD black holes could represent a large increase in the massive black hole number density in the local Universe. Future work can test this hypothesis. We have ongoing observing programmes to obtain similar observations to the ones presented here in four additional massive UCDs, and in the most massive star clusters in the Local Group. However, dynamical detection of black holes will be challenging in all but the brightest and nearest of objects, so accretion signatures[29] or tidal disruption events[30] may represent the best possibility for detecting black holes in less-massive UCDs.

1. Brodie, J. P., Romanowsky, A. J., Strader, J. & Forbes, D. A. The relationships among compact stellar systems: a fresh view of ultracompact dwarfs. *Astron. J.* **142,** 199 (2011).
2. Mieske, S. *et al.* On central black holes in ultra-compact dwarf galaxies. *Astron. Astrophys.* **558,** A14 (2013).
3. Frank, M. J. *et al.* Spatially resolved kinematics of an ultracompact dwarf galaxy. *Mon. Not. R. Astron. Soc.* **414,** L70–L74 (2011).
4. Dabringhausen, J., Kroupa, P., Pflamm-Altenburg, J. & Mieske, S. Low-mass X-ray binaries indicate a top-heavy stellar initial mass function in ultracompact dwarf galaxies. *Astrophys. J.* **747,** 72 (2012).
5. Strader, J. *et al.* The densest galaxy. *Astrophys. J.* **775,** L6 (2013).
6. Blakeslee, J. P. *et al.* The ACS Fornax cluster survey. V. Measurement and recalibration of surface brightness fluctuations and a precise value of the Fornax–Virgo relative distance. *Astrophys. J.* **694,** 556–572 (2009).
7. Schwarzschild, M. A numerical model for a triaxial stellar system in dynamical equilibrium. *Astrophys. J.* **232,** 236–247 (1979).
8. van den Bosch, R. C. E., van de Ven, G., Verolme, E. K., Cappellari, M. & de Zeeuw, P. T. Triaxial orbit based galaxy models with an application to the (apparent) decoupled core galaxy NGC 4365. *Mon. Not. R. Astron. Soc.* **385,** 647–666 (2008).
9. van den Bosch, R. C. E. & de Zeeuw, P. T. Estimating black hole masses in triaxial galaxies. *Mon. Not. R. Astron. Soc.* **401,** 1770–1780 (2010).
10. Kormendy, J. & Ho, L. C. Coevolution (or not) of supermassive black holes and host galaxies. *Annu. Rev. Astron. Astrophys.* **51,** 511–653 (2013).
11. Reines, A. E., Greene, J. E. & Geha, M. Dwarf galaxies with optical signatures of active massive black holes. *Astrophys. J.* **775,** 116 (2013).
12. Gebhardt, K., Rich, R. M. & Ho, L. C. An intermediate-mass black hole in the globular cluster G1: improved significance from new Keck and Hubble Space Telescope observations. *Astrophys. J.* **634,** 1093–1102 (2005).
13. Jalali, B. *et al.* A dynamical N-body model for the central region of ω Centauri. *Astron. Astrophys.* **538,** A19 (2012).
14. van der Marel, R. P. & Anderson, J. New limits on an intermediate-mass black hole in Omega Centauri. II. Dynamical models. *Astrophys. J.* **710,** 1063–1088 (2010).
15. Miller-Jones, J. C. A. *et al.* The absence of radio emission from the globular cluster G1. *Astrophys. J.* **755,** L1 (2012).
16. van den Bosch, R. C. E. *et al.* An over-massive black hole in the compact lenticular galaxy NGC 1277. *Nature* **491,** 729–731 (2012).
17. Gallo, E. *et al.* AMUSE-Virgo. II. Down-sizing in black hole accretion. *Astrophys. J.* **714,** 25–36 (2010).
18. Ho, L. C. Nuclear activity in nearby galaxies. *Annu. Rev. Astron. Astrophys.* **46,** 475–539 (2008).
19. Mieske, S., Hilker, M. & Misgeld, I. The specific frequencies of ultra-compact dwarf galaxies. *Astron. Astrophys.* **537,** A3 (2012).
20. Drinkwater, M. J. *et al.* A class of compact dwarf galaxies from disruptive processes in galaxy clusters. *Nature* **423,** 519–521 (2003).
21. Pfeffer, J. & Baumgardt, H. Ultra-compact dwarf galaxy formation by tidal stripping of nucleated dwarf galaxies. *Mon. Not. R. Astron. Soc.* **433,** 1997–2005 (2013).
22. Portegies Zwart, S. F., Baumgardt, H., Hut, P., Makino, J. & McMillan, S. L. W. Formation of massive black holes through runaway collisions in dense young star clusters. *Nature* **428,** 724–726 (2004).
23. Graham, A. W. & Spitler, L. R. Quantifying the coexistence of massive black holes and dense nuclear star clusters. *Mon. Not. R. Astron. Soc.* **397,** 2148–2162 (2009).
24. Ferrarese, L. *et al.* A fundamental relation between compact stellar nuclei, supermassive black holes, and their host galaxies. *Astrophys. J.* **644,** L21–L24 (2006).
25. Côté, P. *et al.* The ACS Virgo cluster survey. VIII. The nuclei of early-type galaxies. *Astrophys. J.* **165** (suppl.), 57–94 (2006).
26. Turner, M. L. *et al.* The ACS Fornax cluster survey. VI. The nuclei of early-type galaxies in the Fornax cluster. *Astrophys. J.* **203** (suppl.), 5 (2012).
27. Strader, J., Caldwell, N. & Seth, A. C. Star clusters in M31. V. Internal dynamical trends: some troublesome, some reassuring. *Astron. J.* **142,** 8 (2011).
28. Bastian, N., Covey, K. R. & Meyer, M. R. A universal stellar initial mass function? A critical look at variations. *Annu. Rev. Astron. Astrophys.* **48,** 339–389 (2010).
29. Gültekin, K., Cackett, E. M., King, A. L., Miller, J. M. & Pinkney, J. Low-mass AGNs and their relation to the fundamental plane of black hole accretion. *Astrophys. J.* **788,** L22 (2014).
30. Miller, M. C., Farrell, S. A. & Maccarone, T. J. A wind accretion model for HLX-1. *Astrophys. J.* **788,** 116 (2014).

Author Contributions All authors helped with interpretation of the data and provided comments on the manuscript. A.C.S. planned observations, reduced and analysed the data and was the primary author of the text. R.v.d.B. created dynamical models and contributed text. S.M. contributed text. H.B. ran tidal stripping simulations. M.d.B. created dynamical models and analysed model results. J.S., N.N., and R.M. helped to plan the observations. I.C. helped verify kinematic measurements. M.H. and L.S. helped with the compilation of UCD numbers.

METHODS

Here we discuss the details of our data, the kinematics and the modelling of the light profile. We then provide details on the dynamical modelling and discuss alternatives to a supermassive black hole. The Supplementary Information has additional information on our calculation of the number of black holes in UCDs compared to galaxies and details on our simulations showing that M60-UCD1 is consistent with being a 10^{10} $M_\odot$ galaxy tidally stripped by M60.

Gemini/NIFS data. The kinematic data presented here are derived from integral field spectroscopic observations of M60-UCD1 taken on 20 February, 18 May and 19 May 2014 using Gemini/NIFS[31] using the Altair laser guide star adaptive optics with an open loop focus model. Gemini/NIFS provides infrared spectroscopy in $0.1'' \times 0.04''$ pixels over a 3″ field of view; our observations were taken in the K band at wavelengths of 2.0–2.4 μm.

The final data cube was made from a total of nine 900-s on-source exposures with good image quality (four taken on 20 February, four on 18 May and one on 19 May). Data were taken in the order: object–sky–object. The sky frames were taken with small ~10″ offsets from the source at similar galactocentric radii within M60. Large diagonal ~1″ dithers made between the two neighbouring object exposures ensure that the same sky pixels were not used even when the data are binned, thus improving our signal-to-noise ratio.

The Gemini/NIFS data were reduced similarly to in our previous work with NIFS[32]. Each individual data cube was corrected using an A0V telluric star (HIP 58616) at similar air mass. However, owing to an error, no telluric star was observed on 20 February so the telluric from 18 May was used to correct that exposure as well; below we test any effects this may have on our kinematic data and show that they are minimal. The Gemini NIFS pipeline was modified to enable proper error propagation and additional codes written in the Interactive Data Language were used to combine the final data cube including an improved outlier rejection algorithm that uses neighbouring pixels to help determine bad pixels. Each dithered data cube was shifted and combined to yield a final data cube with $0.05'' \times 0.05''$ spatial pixels; a velocity offset to compensate for the differing barycentric corrections was applied to the February cubes. The final signal-to-noise ratio in the central pixels is ~60 per resolution element at $\lambda = 2,350$ nm.

The instrumental dispersion of NIFS varies by ~20% across the field of view. To determine the instrumental dispersion of each spatial pixel, the sky frame exposures were dithered and combined identically to the science images. Using this sky data cube, we fitted isolated OH sky lines in each spatial pixel using double Gaussian fits to derive the instrumental dispersion; the median FWHM was 0.421 nm.

The point spread function (PSF) was derived using an image from the Hubble Space Telescope's Advanced Camera for Survey Wide Field Channel (Program ID: 12369). This image was convolved to match the continuum emission in the NIFS data cube. We used a Lucy–Richardson deconvolved version of the Hubble Space Telescope image in the F475W filter; the available F850LP filter image is closer in wavelength, but has a significantly more complicated and less well modelled PSF. The deconvolved F475W image was then fitted to our NIFS image using the MPFIT2DFUN code (http://physics.wisc.edu/~craigm/idl/fitting.html). A double Gaussian model was required to obtain a good fit to the PSF; the inner component has a FWHM of $0.155''$ and contains 55% of the light while the outer component has a FWHM of $0.62''$ and contains 45% of the light. The residuals to the fit have a standard deviation of just 6% out to a radius of $1''$. This PSF was assumed for the kinematics in all dynamical models.

Deriving the kinematics. The kinematics were determined by fitting the CO bandhead region (2.295–2.395 μm) to stellar templates[33] using the penalized pixel-fitting algorithm PPXF[34]. We fitted the radial velocity V, dispersion σ, skewness h_3 and kurtosis h_4 to the data. Before fitting, the data were binned together using Voronoi binning[35] to achieve signal-to-noise ratios of >35 per resolution element in each bin. The Voronoi bins at large radii were predominantly radial in shape, and thus beyond $0.5''$ we binned spectra using elliptical sections with an axial ratio of 0.85 on the basis of the observed ellipticity at these radii in the Hubble Space Telescope images. These outer bins have signal-to-noise ratios between 24 and 42 per resolution element. An example of kinematic fits in a high dispersion central pixel and low dispersion outer bin are shown in Extended Data Fig. 1. To determine errors on the derived kinematics in each bin, Monte Carlo estimates were performed by adding Gaussian random noise to each spectral pixel in each bin, refitting the kinematics and then taking the standard deviation of the resulting data. The central velocity of M60-UCD1 is found to be $1,294 \pm 5\,\mathrm{km\,s}^{-1}$, while the integrated dispersion at $r < 0.75''$ is found to be $69 \pm 1\,\mathrm{km\,s}^{-1}$. Both values are consistent with the integrated optical spectroscopy measurements[5]. The kinematic maps in all four velocity moments are shown in Extended Data Fig. 2.

The robustness of the kinematic measurements and their errors was tested by comparing the data taken on 20 February with the data taken in May. The four February and five May cubes were combined into separate final cubes. Spectra were then extracted in the same bins as used for the full data set. We compared the velocity and dispersion differences between the cubes to the differences expected from the errors and found that these were consistent. More explicitly, we found that the distribution of $\left(V_{\mathrm{May}} - V_{\mathrm{Feb}}\right)\Big/\sqrt{\mathrm{Error}_{\mathrm{May}}^2 + \mathrm{Error}_{\mathrm{Feb}}^2}$ had a standard deviation between 0.9 and 1.1 for both velocity and dispersion measurements; the bias between the two measurements was less than the typical errors on the measurements. We also tested for template mismatch using PHOENIX model spectra[36] and find consistent kinematic results within the errors. Thus we conclude that (1) our kinematic measurements are robust and (2) our kinematics errors are correctly estimated.

Multi-Gaussian expansion model of M60-UCD1. Archival Hubble Space Telescope data in the F475W (g) filter (Program ID: 12369) provide the cleanest measurement of the light distribution of M60-UCD1. We first fitted the data to a PSF-convolved two-component Sérsic profile using methods and profiles similar to previous fits of M60-UCD1[5]. To enable the fitting of axisymmetric models (see below), we forced the outer nearly circular component (with axial ratio $b/a \approx 0.95$) to be exactly circular to ensure that the model had no isophotal twist caused by a misalignment of the inner and outer component. Enforcing circularity in the outer component had a negligible effect on the quality of fit compared to the previous best-fitting model[5]. Our best-fitting axisymmetric model has an outer Sérsic component (circular) with surface brightness $\mu_e = 20.09$, effective radius $r_e = 0.''600$, Sérsic $n = 1.20$ and integrated magnitude $g = 18.43$, and an inner Sérsic component with position angle PA $= -49.45$, $b/a = 0.749$, $\mu_e = 17.322$, $r_e = 0.175''$, $n = 3.31$ and $g = 18.14$. We generated a multi-Gaussian expansion[37,38] of this profile for use in our dynamical models. The multi-Gaussian expansion values are shown in Extended Data Table 1.

We note that data in the F850LP filter of M60-UCD1 is also available, but due to the lack of a red cutoff on the filter the PSF is asymmetric, temperature dependent, and difficult to characterize. The one downside of using the F475W filter is that it is at a significantly different wavelength than the kinematic measurements. However, there is no evidence for any colour variation within the object; the inner and outer morphological components have consistent colours within 0.01 mag (filter magnitudes F475W minus F850LP = 1.56 and 1.57 for the inner and outer components respectively). The radial profile of deconvolved F475W and F850LP images is flat; any colour differences are $\lesssim 0.03$ mag. Thus there is no evidence for any stellar population differences within the object.

Dynamical modelling. The most common method for measuring dynamical black hole masses is Schwarzschild orbit-superposition modelling[7] of the stellar kinematics. Here we use a triaxial Schwarzschild code described in detail in ref. 8. To briefly summarize the method, the dynamical models are made in three steps. First, a three-dimensional luminous mass model of the stars is made by de-projecting the two-dimensional light model from the Hubble Space Telescope image. This is done with the multi-Gaussian expansion from the previous section, which is deprojected to construct a three-dimensional mass distribution for the stars, assuming a constant mass-to-light ratio and a viewing angle. Second, the gravitational potential is inferred from the combination of the stellar mass and the black hole mass. In a triaxial potential, the orbits conserve three integral of motions that can be sampled by launching orbits orthogonally from the x–z plane. A full set of representative orbits are integrated numerically, while keeping track of the paths and orbital velocities of each orbit. The orbit library we used for M60-UCD1 consists of 7,776 orbits. Third, we model the galaxy by assigning each orbit an amount of light, simultaneously fitting both the total light distribution and the NIFS stellar kinematics (Extended Data Fig. 2) including the effects of the PSF given above. Each of these steps is then repeated with different viewing angles and potentials to find the best-fitting mass distribution and confidence intervals. The recovery of the internal dynamical structure (distribution function), intrinsic shape, and black hole mass using this code are validated in a series of papers[9,39,40]. The orbit-based models are fully self-consistent and allow for all physically possible anisotropies; the models make no a priori assumptions about the orbital configuration.

For modelling M60-UCD1, we adopted a (nearly) oblate geometry with an intermediate axis ratio of $b/a = 0.99$. In total there are three free parameters: the stellar M/L, the black hole mass, and the viewing angle. A total of 62 different stellar M/L ratios, sampled in linear steps, and 22 black hole masses, sampled in logarithmic steps, were modelled at four inclinations between 41 and 85 degrees to sample the intrinsic flattening of the shortest to longest axis, c/a, between 0.13 and 0.73. The individual grid points sampled are shown in Fig. 3. We note that the observed rotation does not appear to rotate cleanly around the short axis, as the zero-velocity curve appears to twist at $0.3''$. This may suggest that the object is mildly triaxial, but this has minimal impact on our determination of the black hole mass and stellar M/L. More significant is the increasing roundness of M60-UCD1 at large radii, which is fitted by our modelling.

The NIFS kinematics is used by the model to constrain the total mass distribution. The confidence contours shown in Fig. 3 of the main paper are marginalized over inclination and are based on fits to point symmetrized kinematic data[9]. Error bars are determined for the remaining two degrees of freedom, with $\Delta\chi^2 = 2.30$,

6.18 and 11.83 corresponding to 1σ, 2σ and 3σ. The best-fitting constant M/L model with no black hole has $\Delta\chi^2 = 20.0$, and thus is excluded at more than 4σ. The reduced χ^2 of the best-fitting model to the unsymmetrized data are 0.96 for 280 observables and three parameters. The best-fitting inclination is only constrained to be $>50°$. Such a weak constraint on the viewing angle is usual for dynamical models[40]. There is no dust disk present in this object that can help to constrain the inclination. We note that the maximum M/L ratio expected for an old stellar population with solar metallicity and a canonical initial mass function is $\sim$4.1 in the V band and $\sim$5.1 in the g band[2]. This value is somewhat higher than the best-fitting $M/L_g \approx 3.6$, but is allowed at $\sim 2\sigma$ (see Fig. 3).

The ability to detect a black hole with a given set of observations is often quantified by calculating the sphere of influence of the black hole. While the sphere of influence is normally calculated based on the dispersion of the object, the large black hole mass fraction in M60-UCD1 makes the enclosed mass definition of the gravitational sphere of influence $M_{star}(r < r_{infl}) = 2M_{bh}$ more comparable to previous r_{infl} measurements[41]. Using this definition, we find $r_{infl} = 0.27''$. Following the convention presented in a recent review of black hole masses[10], we obtain $r_{infl}/\sigma^* \approx 4$, where σ^* is the resolution of our PSF core. We have many independent measurements of the kinematics within this radius.

The dynamics show that this object has a multi-component structure. In the phase space there are several components visible (Extended Data Fig. 3). Roughly 70% of the stars are on co-rotating orbits, but the remainder are evenly split between counter-rotating and non-rotating, radial, orbits. This indicates that this object was not formed in a single formation event. The co-rotating orbits dominate at smaller radii, while at larger radii both co-rotating and non-rotating orbits are seen. This corresponds well to the two-component structure fit to the integrated light where we find an inner component with an axial ratio $b/a = 0.75$ and an outer component that is nearly round[5]. The anisotropy $\beta \equiv 1 - \sigma_{radial}^2 / \sigma_{tangential}^2$ is nearly isotropic and does not significantly vary as function of radius. On the other hand $\beta_z \equiv 1 - \sigma_R^2/\sigma_z^2$ (where R and z are cylindrical coordinates) gradually decreases outwards from 0 to smaller than -1 and is thus strongly negative. The anisotropy profiles and orbit types are shown in Extended Data Fig. 4. As expected in an (nearly) oblate system the orbits are dominated by short-axis tubes, apart from the region near the black hole where the radial orbits take over.

One of the most critical assumptions we make in these best-fitting models is the assumption of a constant M/L. This is a well justified simplification for M60-UCD1. As discussed above, there is no evidence for any radial colour variation, suggesting a stellar population with a constant age. Furthermore, the formal age estimate from spectral synthesis measurements of integrated optical spectra is 14.5 ± 0.5 billion years (Gyr) (ref. 5), leaving little room for any contribution from young populations with significant M/L differences. Radial variations in the initial mass function that would leave the colour unchanged are not excluded a priori but are highly unlikely, as discussed below.

To test our modelling, we also ran Jeans models using the JAM code[42]. These models have been shown in the past to give consistent results in comparisons with Schwarzschild models[43]. However, we also note that the JAM models enforce a simpler and not necessarily physical orbital structure, including a constant anisotropy aligned with cylindrical coordinates. Furthermore, the Jeans models do not fit the full line-of-sight velocity distribution, as the Schwarzschild models do. JAM models were run over a grid of black hole mass, M/L_g, anisotropy β, and inclination i. Fitting only the second moments (the root-mean-square velocity $V_{RMS} = \sqrt{V^2 + \sigma^2}$), we obtain a best-fitting stellar dynamical $M/L_g = 2.3 \pm 0.9$ and $M_{bh} = 2.4 \pm 0.4 \times 10^7 M_\odot$ marginalizing over the other two parameters. The 1σ error bars given here were calculated assuming $\Delta\chi^2 < 2.30$ to give comparable error bars to the Schwarzschild models. The fit is relatively insensitive to the other two parameters, with β_z varying between -1 and 0 and i between $50°$ and $90°$. These models are fully consistent with the Schwarzschild models fits. A JAM model with zero black hole mass is strongly excluded in the data with $\Delta\chi^2 > 46$ and a best-fitting stellar dynamical $M/L_g \approx 6.5$.

We also use the Jeans modelling to investigate fully isotropic models. Isotropy is observed in the central parsec of the Milky Way[44], the only galaxy nucleus where three-dimensional velocities for individual stars have been measured. Furthermore, isotropy has been assumed in the modelling of possible black holes in UCDs[2]. Interestingly, the V_{RMS} data of M60-UCD1 is also fully consistent with an isotropic model with a $\chi^2 - \chi_{min}^2 = 1.1$ (within the 1σ contour). This is consistent with the Schwarzschild models, which find that the system is close to isotropic with $\beta \approx 0.0$. The best-fitting isotropic Jeans model has a black hole mass of $2.2 \pm 0.4 \times 10^7 M_\odot$ and $M/L_g = 2.8 \pm 0.7$.

Dark matter and alternatives to a black hole. We now discuss the possible dark matter content of M60-UCD1 and consider whether an alternative scenario could explain the kinematics of M60-UCD1 without a supermassive black hole.

Dark matter is not expected to make a significant contribution to the kinematics of M60-UCD1. This is due to the extremely high stellar density; dissipationless dark

matter cannot achieve anywhere close to the same central densities as baryonic matter. This is shown clearly in previous work matching dark matter halos to galaxies[45]. For realistic dark matter halo profiles, even a $10^{13} M_\odot$ halo would have only $10^7 M_\odot$ within the central 100 pc, while a $10^{14} M_\odot$ halo would be required to have just $10^6 M_\odot$ within M60-UCD1's effective radius; thus even such a massive halo (about three orders of magnitude more massive than would be expected for a galaxy with a stellar mass of about $10^{10} M_\odot$) would contribute only around 1% to M60-UCD1's mass. More importantly, a dark matter halo would contribute an extended distribution of mass and fail to produce the central rise in the velocity dispersion. We note that the one previous resolved measurement of UCD kinematics[3] found no evidence for dark matter in a significantly more extended UCD. Including dark matter in our dynamical models would slightly decrease the stellar M/L, which in turn would further increase the inferred black hole mass in this object.

An alternative to a massive black hole could be a centrally enhanced M/L. To test this scenario we constructed dynamical models without a black hole, but with a radial M/L gradient increasing towards the centre. We found that the models with an M/L slope of -0.44 ± 0.16 in log(radius) can yield a good fit, with a $\Delta\chi^2$ difference of 3 from the best-fitting constant M/L + black hole model. This indicates that a model without a black hole and with a M/L gradient is allowed at 2σ. However, in addition to providing a slightly worse formal fit to the data, the M/L gradient model is also less physically plausible than the presence of a supermassive black hole. The log(r) dependence means that the centre has a very large M/L. This is shown clearly in Extended Data Fig. 5. Within our central resolution element ($r \approx 5$ pc), the M/L_g in this model is $\sim$12 compared to a value of $\sim$2 at 100 pc. The model is thus replacing the black hole mass with stellar mass near the centre in order to match the kinematic data.

This dramatic M/L gradient cannot be due to stellar age variations, given M60-UCD1's uniform colour. The M/L at $r < 5$ pc is a factor of more than 2 above that expected for an old stellar population with a canonical initial mass function (see above) and thus would require that more than half of the approximately $3.5 \times 10^7 M_\odot$ inside that radius be in low-mass stars or stellar remnants that produce little light[4,46]. We note that dynamical mass segregation is not expected to occur in M60-UCD1, because the half-mass relaxation time is about 350 Gyr and remains more than 10 Gyr at smaller radii[41,47]. Thus the only way to explain the M/L gradient would be to have extreme radial variations in the initial mass function. Assuming a change in the high-mass end of the initial mass function (and thus an increase in stellar remnants), the required upper initial mass function slope α (where the slope of the stellar mass function is specified as $dN/dM \propto M^{-\alpha}$) is between 0 and 1.4 at the centre, as opposed to the canonical 2.35 (ref. 48). We consider this possibility very unlikely.

31. McGregor, P. J. et al. Gemini near-infrared integral field spectrograph (NIFS). In *Instrument Design and Performance for Optical/Infrared Ground-based Telescopes* (eds Iye, M. & Moorwood, A. F. M.) *Proc. SPIE* **4841**, 1581–1591 (SPIE, 2003).
32. Seth, A. C. et al. The NGC 404 nucleus: star cluster and possible intermediate-mass black hole. *Astrophys. J.* **714**, 713–731 (2010).
33. Wallace, L. & Hinkle, K. High-resolution spectra of ordinary cool stars in the K band. *Astrophys. J. Suppl. Ser.* **107**, 312–390 (1996).
34. Cappellari, M. & Emsellem, E. Parametric recovery of line-of-sight velocity distributions from absorption-line spectra of galaxies via penalized likelihood. *Publ. Astron. Soc. Pacif.* **116**, 138–147 (2004).
35. Cappellari, M. & Copin, Y. Adaptive spatial binning of integral-field spectroscopic data using Voronoi tessellations. *Mon. Not. R. Astron. Soc.* **342**, 345–354 (2003).
36. Husser, T.-O. et al. A new extensive library of PHOENIX stellar atmospheres and synthetic spectra. *Astron. Astrophys.* **553**, A6 (2013).
37. Emsellem, E., Monnet, G. & Bacon, R. The multi-gaussian expansion method: a tool for building realistic photometric and kinematical models of stellar systems. I. The formalism. *Astron. Astrophys.* **285**, 723–738 (1994).
38. Cappellari, M. Efficient multi-Gaussian expansion of galaxies. *Mon. Not. R. Astron. Soc.* **333**, 400–410 (2002).
39. van de Ven, G., de Zeeuw, P. T. & van den Bosch, R. C. E. Recovery of the internal orbital structure of galaxies. *Mon. Not. R. Astron. Soc.* **385**, 614–646 (2008).
40. van den Bosch, R. C. E. & van de Ven, G. Recovering the intrinsic shape of early-type galaxies. *Mon. Not. R. Astron. Soc.* **398**, 1117–1128 (2009).
41. Merritt, D. *Dynamics and Evolution of Galactic Nuclei* (Princeton Univ. Press, 2013).
42. Cappellari, M. Measuring the inclination and mass-to-light ratio of axisymmetric galaxies via anisotropic Jeans models of stellar kinematics. *Mon. Not. R. Astron. Soc.* **390**, 71–86 (2008).
43. Cappellari, M. et al. Testing mass determinations of supermassive black holes via stellar kinematics. Preprint at http://arxiv.org/abs/1001.3233 (2010).
44. Schödel, R., Merritt, D. & Eckart, A. The nuclear star cluster of the Milky Way: proper motions and mass. *Astron. Astrophys.* **502**, 91–111 (2009).
45. Tollerud, E. J., Bullock, J. S., Graves, G. J. & Wolf, J. From galaxy clusters to ultra-faint dwarf spheroidals: a fundamental curve connecting dispersion-supported galaxies to their dark matter halos. *Astrophys. J.* **726**, 108 (2011).
46. Cappellari, M. et al. Systematic variation of the stellar initial mass function in early-type galaxies. *Nature* **484**, 485–488 (2012).
47. Binney, J. & Tremaine, S. *Galactic Dynamics* 2nd edn (Princeton Univ. Press, 2008).

48. Dabringhausen, J., Kroupa, P. & Baumgardt, H. A top-heavy stellar initial mass function in starbursts as an explanation for the high mass-to-light ratios of ultra-compact dwarf galaxies. *Mon. Not. R. Astron. Soc.* **394,** 1529–1543 (2009).

49. Seth, A. C. Gas accretion in the M32 nucleus: past and present. *Astrophys. J.* **725,** 670–676 (2010).

50. Schlafly, E. F. & Finkbeiner, D. P. Measuring reddening with Sloan Digital Sky Survey stellar spectra and recalibrating SFD. *Astrophys. J.* **737,** 103 (2011).
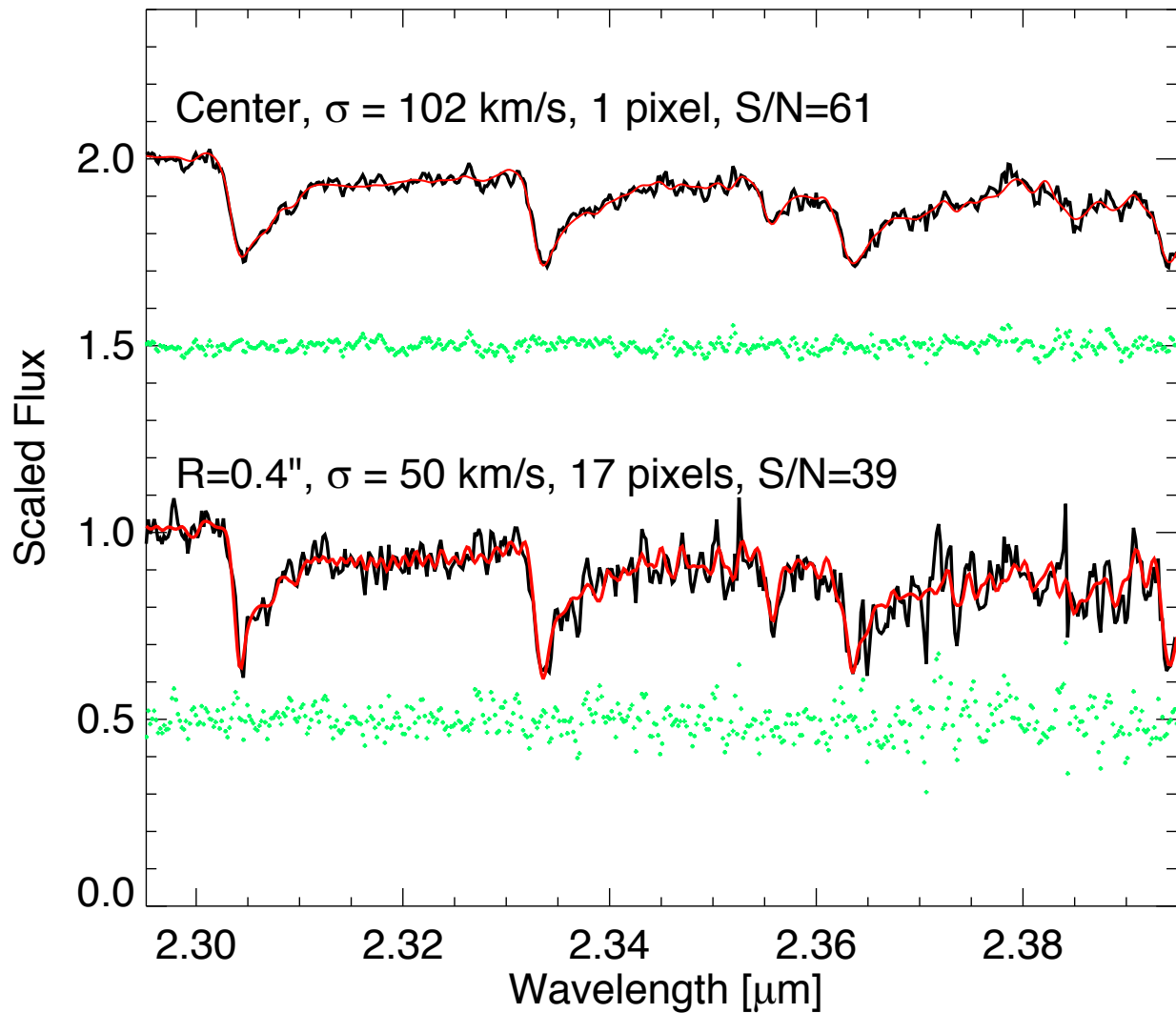
Extended Data Figure 1 | Two example spectra (black lines) and their kinematic fits (red lines). Residuals for both spectra are shown in green. The top spectrum is from one of the central-most pixels and is the spectrum from a single 0.05″ × 0.05″ pixel. The bottom spectrum is at a radius of 0.4″ and is the sum of 17 spatial pixels. Signal-to-noise ratios are given per resolution element. The contrast in dispersion is seen very clearly, with broad smooth lines in the top spectrum and sharper lines in the bottom. Both spectra were normalized to one; the central spectrum was then offset by +1 for visibility. The residuals were offset by 0.5 and 1.5.
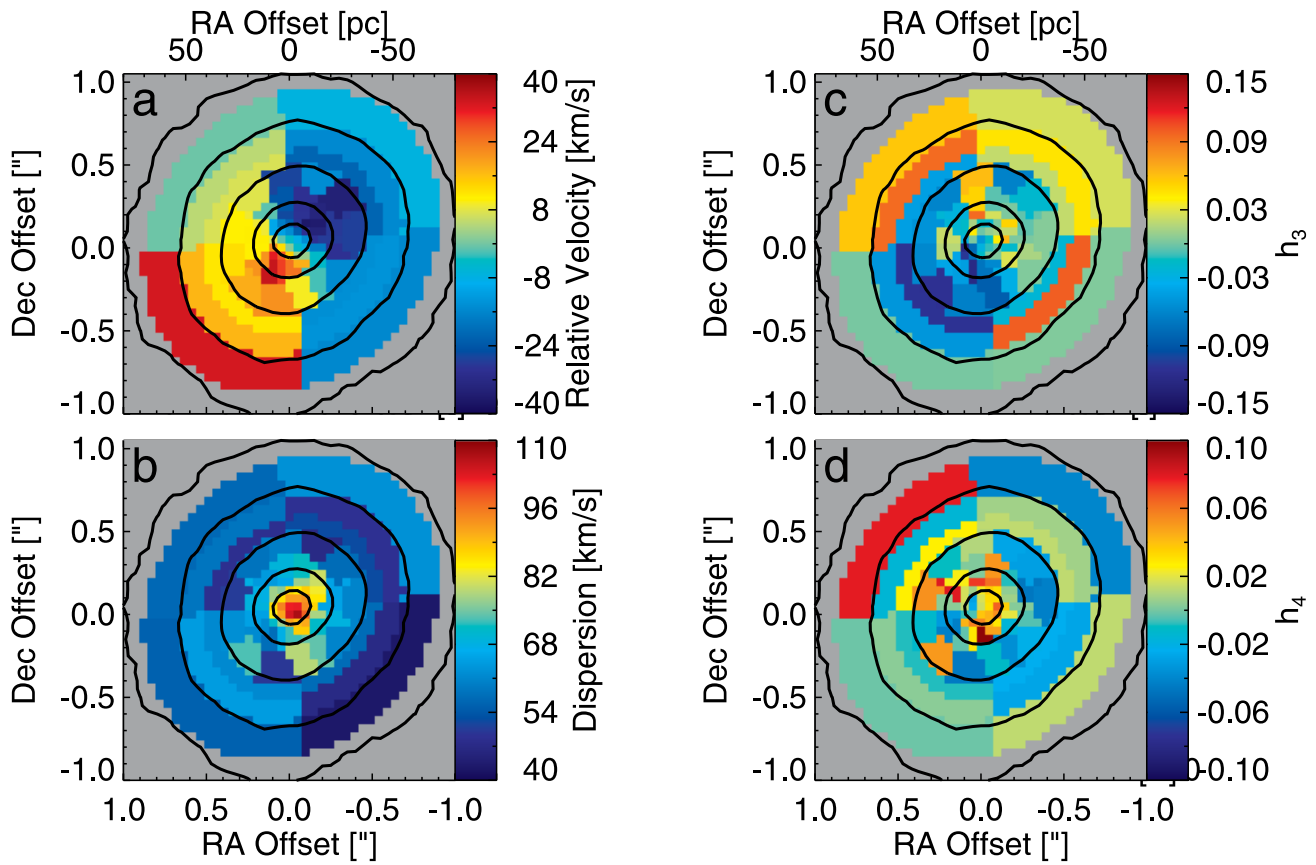
Extended Data Figure 2 | The full results of kinematic fits to M60-UCD1.
a, Radial velocity; **b**, dispersion; **c**, the skewness h_3; **d**, kurtosis h_4. Black contours show the K-band continuum at intervals of 1 mag arcsec^{-2}. The median 1σ errors are 5.8 km s^{-1} for the velocities, 6.8 km s^{-1} for dispersion, 0.06 for h_3 and 0.07 for h_4. The skewness clearly shows the commonly seen anti-correlation with the velocity[49].
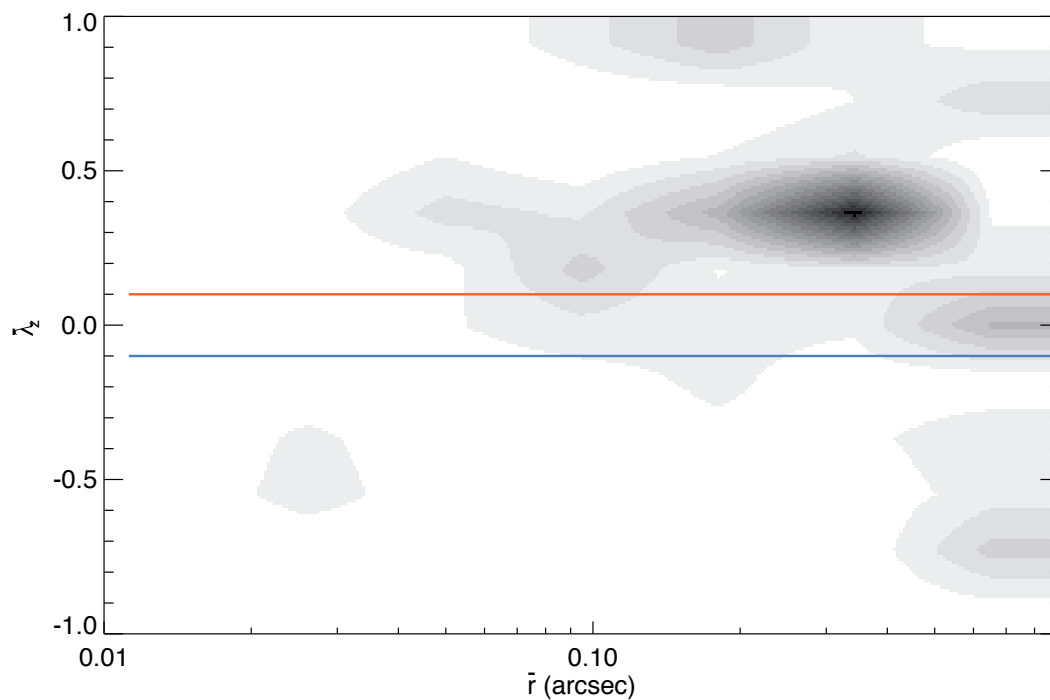
Extended Data Figure 3 | Distribution of mass as function of spin and average radius of the orbits as inferred from the dynamical model. The average spin is defined as $\bar{\lambda}_z = \bar{J}_z \times (\bar{r}/\bar{\sigma})$, where $\bar{J}_z$ is the average angular momentum along the z-direction, $\bar{r}$ is the average radius, and $\bar{\sigma}$ is the average second moment of the orbit. Several distinct components are visible. Although 70% of the mass is on co-rotating orbits with $\bar{\lambda}_z \geq |0.1|$ (shown as red and blue lines), there is also a significant amount of mass in components without rotation and counter-rotation.
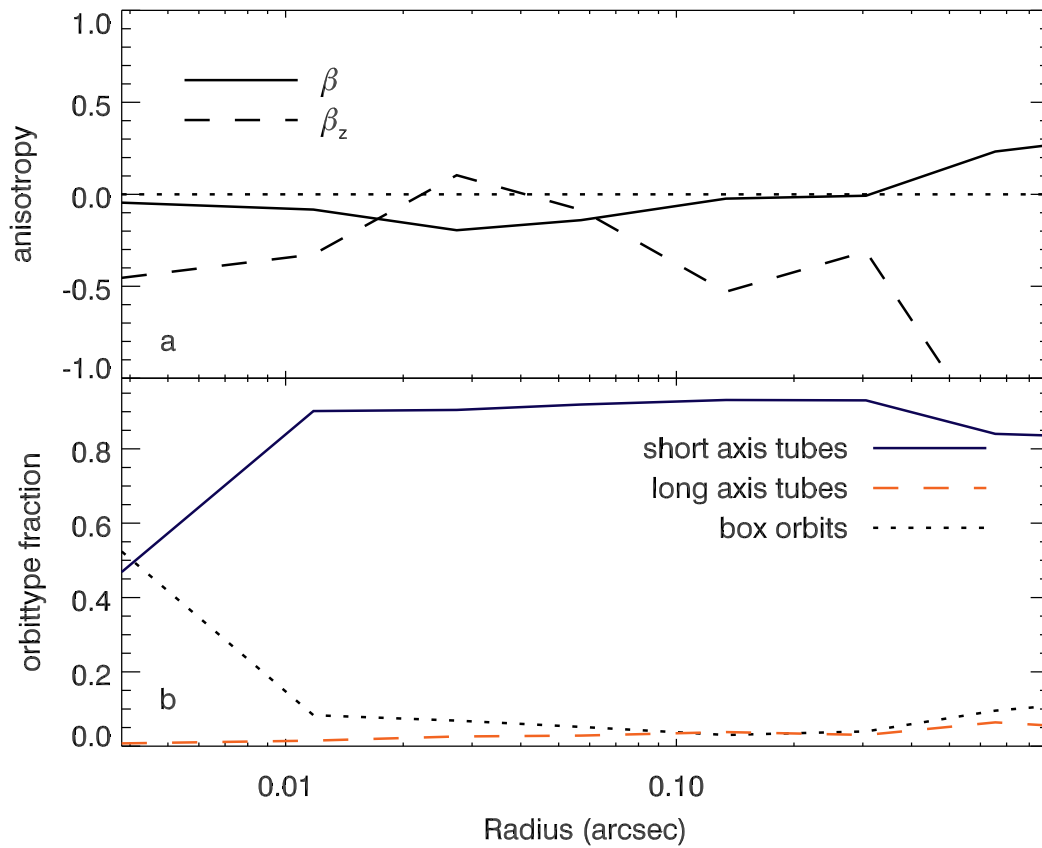
Extended Data Figure 4 | Anisotropy and orbit type distribution as function of radius. a, β and β_z shown as solid and dashed lines, respectively. Anisotropy $\beta \equiv 1 - \sigma^2_{radial} / \sigma^2_{tangential}$ indicates the relative size of the velocity ellipsoid in spherical coordinates and it is relatively constant over the radii probed by the kinematics. On the other hand $\beta_z \equiv 1 - \sigma^2_R / \sigma^2_z$ (in cylindrical units) gradually declines. We note, however, that the velocity ellipsoid cannot be aligned with the cylindrical coordinates throughout a stellar system, and thus a physical interpretation of β_z is not straightforward. **b**, The relative orbit fraction as function of radius.
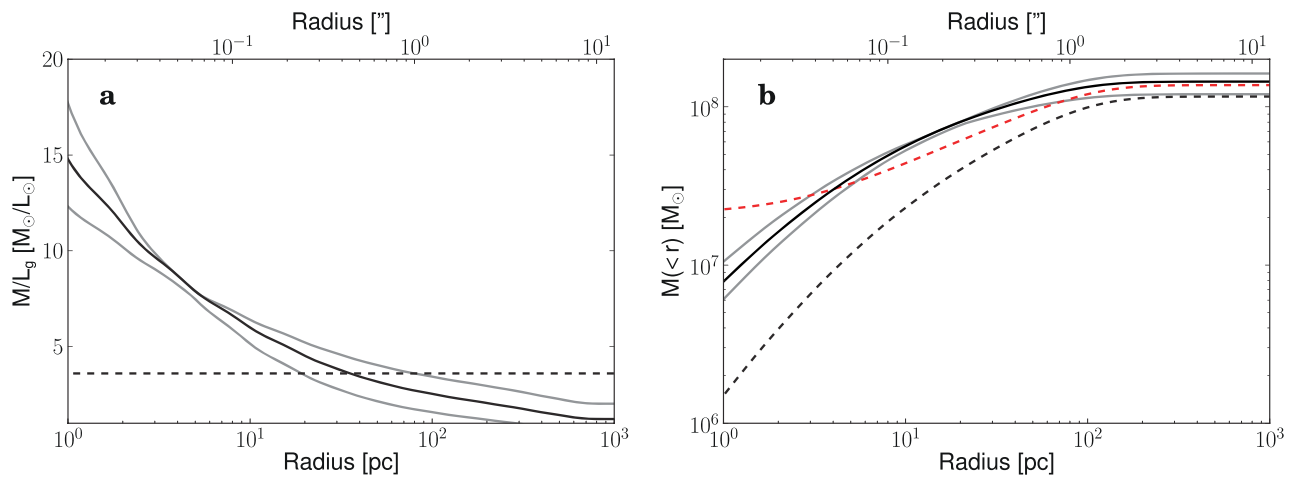
Extended Data Figure 5 | Mass-to-light ratio gradient dynamical models.
a, The solid line shows the best-fitting g-band mass-to-light ratio (M/L_g) for a model that includes an M/L gradient but no black hole. The maximum M/L_g expected for a normal stellar population (assuming a standard IMF and age of 13 Gyr) is $\sim$5.1; the central M/L_g is about three times this value. Grey lines indicate the range of M/L_g values for gradient models within 1σ of the best fit. The dashed line shows the best-fitting constant-M/L model for a model including a supermassive black hole. **b**, The enclosed mass as a function of radius. The variable M/L fit with no black hole is shown as the solid line with uncertainties in grey. The black and red dashed lines show the enclosed stellar mass and the mass including the black hole from the constant-M/L + black hole fit.
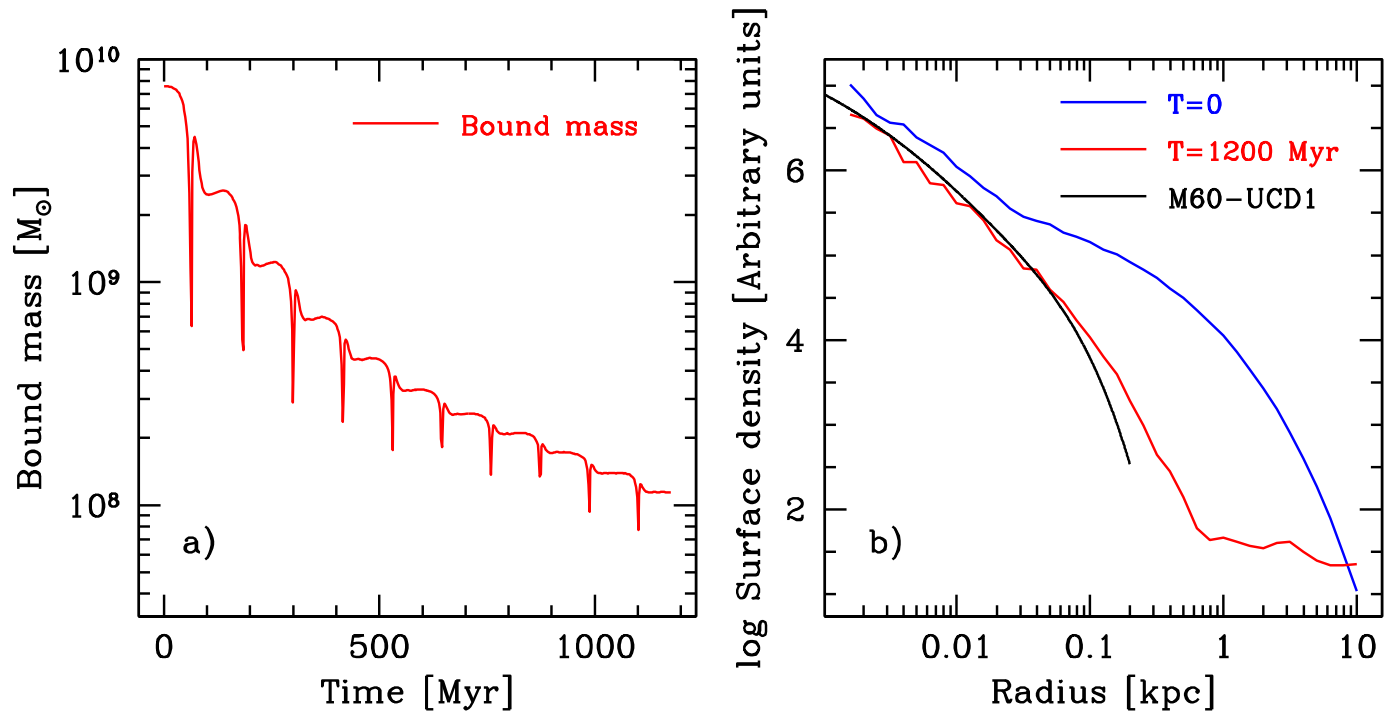
Extended Data Figure 6 | Simulations of tidal stripping. a, The evolution of mass bound to the progenitor as it is being stripped to form a UCD. The progenitor properties were based on estimates from M60-UCD1, while the stripping galaxy is based on the potential of M60. **b**, The density profile evolution of a tidally stripped galaxy that results in a final object similar to that of M60-UCD1.

Extended Data Table 1 | Luminosity model of M60-UCD1

$L_{\odot}pc^{-2}$ (mag)	log σ' (arcsec)	q'
337.276	-1.88135	0.999
651.189	-1.33255	0.999
928.698	-0.918423	0.999
909.443	-0.593469	0.999
554.490	-0.337421	0.999
196.581	-0.131899	0.999
36.1820	0.0420669	0.999
2.26539	0.207857	0.999
374202.	-3.50825	0.749
334899.	-3.08561	0.749
274935.	-2.69367	0.749
204099.	-2.32475	0.749
130962.	-1.98010	0.749
74045.5	-1.66058	0.749
36353.7	-1.35852	0.749
14894.5	-1.07469	0.749
5126.86	-0.808290	0.749
1457.43	-0.558353	0.749
342.689	-0.323720	0.749
65.1802	-0.102248	0.749
10.0077	0.107907	0.749
1.17965	0.316168	0.749
0.0766351	0.553877	0.749

This multi-Gaussian expansion model is composed of 23 Gaussians based on the F475W-band Hubble Space Telescope/ACS image. The position angle of the galaxy is $-49.45°$. The apparent surface brightness (solar luminosity per square parsec) has a correction for galactic foreground extinction (0.087 mag)[50], and assumes a solar luminosity in the g band of 5.12 mag. logσ' is the projected size of each Gaussian on the plane of the sky along the major axis. q' is the projected flattening (the axis ratio of the short to long axis).